# Influence of Pre-Compression on the Ductility of AA6xxx Aluminium Alloys

**B. H. Frodal · K. O. Pedersen · T. Børvik · O. S. Hopperstad**

**Abstract** Reversed loading experiments were conducted to study the influence of pre-compression on the ductility of three aluminium alloys. Diabolo-shaped specimens were machined from extruded profiles along the transverse direction (TD), and heat treated to peak strength (T6 temper). The specimens were subjected to five different levels of pre-compression (0%, 10%, 20%, 30%, 40%), i.e., the specimens were first compressed to a prescribed strain and then pulled to fracture in tension. Using a laser-based measuring system, the minimum diameter in the extrusion direction (ED) and thickness direction (ND) were continuously measured during the tests until fracture. The three aluminium alloys AA6060, AA6082.25 and AA6082.50 had different grain structure and texture. The AA6060 and AA6082.50 alloys had recrystallized grain structure with equi-axed grains and large elongated grains, respectively. The AA6082.25 alloy had a non-recrystallized, fibrous grain structure. It was found that pre-compression has a marked influence on the ductility of the aluminium alloys, which depends on the microstructure and strength of the alloy. Using the compressed configuration as the reference configuration, the relative failure strain could be calculated. For the AA6060 alloy, the relative failure strain increased for increasing pre-compression, and was approximately doubled for 40% pre-compression compared to pure tension. For the AA6082.25 alloy, a slight increase in the relative failure strain was observed for increasing pre-compression, while for the AA6082.50 alloy the relative failure strain was low and approximately constant for different levels of pre-compression.

**Keywords** Aluminium alloys · Ductile fracture · Reversed loading · Pre-compression · Microstructure

B.H. Frodal · T. Børvik · O.S. Hopperstad
Structural Impact Laboratory (SIMLab) and Centre for Advanced Structural Analysis (CASA), Department of Structural Engineering, Norwegian University of Science and Technology (NTNU), NO-7491 Trondheim, Norway
E-mail: bjorn.h.frodal@ntnu.no

K.O. Pedersen
SINTEF Materials & Chemistry, NO-7465 Trondheim, Norway

## 1 Introduction

Ductile fracture is an important field of research, and has been so for many years. The research on ductile fracture has mainly consisted of investigations involving monotonic or proportional loading (e.g. Bao and Wierzbicki 2004; Barsoum and Faleskog 2007; Gao et al. 2009; Gruben et al. 2011, 2012; Graham et al. 2012; Faleskog and Barsoum 2013). In industrial applications the loading path to fracture may not be monotonic or proportional, and information about the influence of non-monotonic and non-proportional loading on the ductile fracture process is needed (Benzerga et al. 2012; Dæhli et al. 2016; Thomas et al. 2016). An important non-proportional loading condition is reversed loading, which is found in many applications, e.g. crushing of tubes, impact against offshore pipelines and some metal forming applications. To gain insight into the mechanisms involved during non-proportional loading, experimental tests are essential.

In the literature, only a few studies have investigated the effect of reversed loading on ductile fracture of aluminium alloys, but for steels there are more studies that have investigated the effect. Ludley and Drucker (1960) used bent-beam tests to reproduce the conditions in pipe impact problems, where the loading history is composed of compression-tension loading. For an estimated pre-compression of 60%, a ductile-to-brittle transition was observed at room temperature. Drucker et al. (1960) stretched axisymmetric smooth tensile specimens machined from cylinders first pre-compressed in the range of 10% to 45%. The cylinders were compressed in increments of approximately 3%, and after each increment

the cylinders were machined to their original shape to ensure as uniform compression as possible. They observed that for increasing pre-compression the tensile strain to failure decreased for the steel.

Enami (2005) investigated the effect of pre-compression on two different steels. For the SM490B steel, cleavage fracture and reduced ductility were observed after pre-compression, while for the TMCP steel, pre-compression did not reduce the ductility, and no evidence of cleavage cracks was found. Bouchard et al. (2008) tested two different steels subjected to reversed loading using diabolo-shaped specimens. They found that pre-compression increased the ductility of both materials, but that the increase was largest for the most anisotropic material. Marcadet and Mohr (2015) performed reversed loading tests on notched flat specimens from a dual phase steel sheet. They used a floating anti-buckling device to achieve pre-strains of up to 13%, and observed an increase in ductility after pre-compression.

Kristoffersen et al. (2013) investigated the effect of pre-compression on an X65 steel used in offshore pipelines, using diabolo-shaped specimens pre-compressed up to 100%. They found that the ductility of the steel increased for 10% pre-compression, but decreased for higher levels of pre-compression, and observed cleavage fracture for extensive pre-compressions. Further, Kristoffersen et al. (2016) used unit cell simulations to study the fracture mechanisms after pre-compression. The unit cell simulations predicted an increase in ductility after pre-compression unlike the experimental results for pre-compressions larger than 10%. The discrepancy between the unit cell simulations and the experimental results was ascribed to the different fracture mode, namely cleavage fracture, triggered by the pre-compression for the X65 steel.

For aluminium alloys, Bao and Treitler (2004) investigated the ductile crack formation in diabolo-shaped specimens of an AA2024-T351 aluminium alloy subjected to reversed loading. Three different diabolo-shaped geometries were investigated to study the effect of different stress triaxiality. They found that pre-compression reduced the ductility of the alloy for all the geometries tested. The reduced ductility after pre-compression was attributed to particle fracture and an increased dislocation density after pre-compression, which accelerated the void nucleation, growth and coalescence in the succeeding tension stage. They also noted that the AA2024-T351 aluminium alloy had no initial porosity and that the effect of pre-compression might be different for materials with an initial porosity.

Papasidero et al. (2015) studied the effect of stress state and loading path on the ductile fracture of the same AA2024-T351 aluminium alloy. They performed torsion/compression/tension experiments on tubular specimens. What they observed was that both pre-torsion and pre-compression increased the ductility of the alloy, and for compression-tension loading the strain to fracture was increased by 80%.

During reversed loading tests, several important effects can be observed such as the Bauschinger effect and the strength differential (SD) effect. The SD effect denotes the difference in yield strength in compression and tension and it might be coupled with the pressure dependency of materials. Spitzig et al. (1975) investigated two steels under superimposed hydrostatic pressure, tested in tension and compression. The yield and flow stress were sensitive to hydrostatic pressure, but the work-hardening and SD effect were relatively insensitive. Spitzig and Richmond (1984) studied the pressure dependency and the SD effect of an AA1100 aluminium alloy with an initial yield stress of approximately 25 MPa. They found an SD effect of 0.3%, and further that the alloy had a substantial pressure dependency.

In the present paper, the aim is to study the influence of pre-compression on the ductility of three aluminium alloys, i.e., to investigate the influence of pre-compression on the strain to failure. To study this influence, reversed loading experiments have been conducted, where diabolo-shaped specimens were compressed to a predefined strain, and then pulled to fracture in tension. In addition, tests have been performed to study the microstructure at different strain levels during the reversed loading. These tests were then used to identify possible physical mechanisms involved in the ductile fracture process.

## 2 Materials

Three aluminium alloys AA6060, AA6082.25 and AA6082.50 were used in the reversed loading tests. The chemical compositions of the alloys in weight percent are given in Table 1. The main difference between the AA6082.25 and AA6082.50 alloys is that chromium has been added to the former to prevent recrystallization in combination with manganese. The alloys were provided by Hydro Aluminium and were cast in a laboratory casting machine into billets of 200 mm in diameter. These billets were extruded in an industrial extrusion press into rectangular profiles with a thickness of 10 mm and a width of 83 mm. The billets were homogenised and extruded using industrial practice. Diabolo-shaped specimens were machined from the extruded profiles, where the specimens' tensile axis was oriented along the transverse direction (TD) of the extruded profile. After machining, the specimens were solution heat-treated, rapidly quenched in water and artificially aged to peak strength (T6 temper) through five stages: the specimens were 1) kept for 15 min in a salt bath at 540 °C, 2) quenched in water, 3) stored for 15 min in room temperature, 4) kept for five hours in an oil bath at 185 °C, and 5) air cooled to room temperature.

Table 1: Chemical compositions of the aluminium alloys in wt%

| Alloy | Fe | Si | Mg | Mn | Cr | Cu | Zn | Ti | Al |
|-------|-------|-------|-------|-------|-------|-------|-------|-------|------|
| AA6060 | 0.193 | 0.422 | 0.468 | 0.015 | 0.000 | 0.002 | 0.005 | 0.008 | Bal. |
| AA6082.25 | 0.180 | 0.880 | 0.600 | 0.530 | 0.150 | 0.020 | 0.005 | 0.011 | Bal. |
| AA6082.50 | 0.200 | 1.020 | 0.670 | 0.540 | 0.001 | 0.003 | 0.005 | 0.010 | Bal. |

Fig. 1 presents equivalent stress versus equivalent plastic strain curves calibrated from smooth axisymmetric tensile specimens of the three alloys, see Khadyko et al. (2014) for the experimental-numerical procedure. The smooth axisymmetric specimens were oriented along the TD of the extruded profiles. The curves are plotted until the point of failure in the experiments. There is a marked difference in stress level between the alloys, with the AA6060 alloy exhibiting the lowest and the two AA6082 alloys the highest stress levels. The stress level for the two AA6082 alloys is similar. Initially the stress level is approximately 1.8 times higher than for the AA6060 alloy. The work-hardening of the AA6060 and AA6082.25 alloys is similar, while the AA6082.50 has a lower work-hardening rate. There is a marked difference in the failure strain between the alloys. The failure strain for the AA6060 alloy is approximately two times higher than for the AA6082.25 alloy, which is approximately three times higher than for the AA6082.50 alloy.
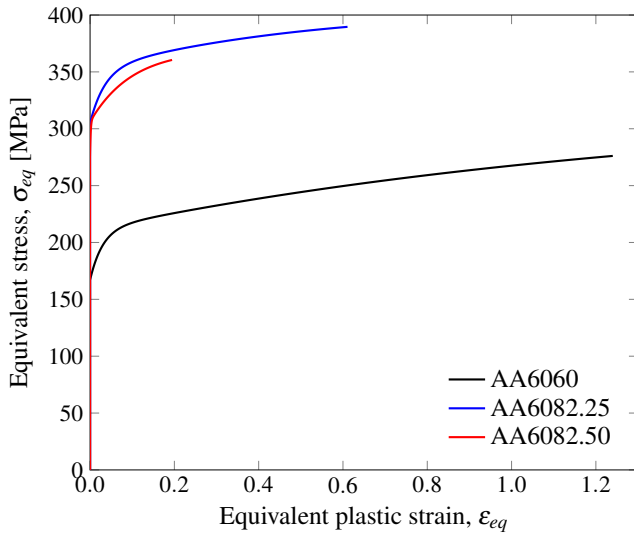
## 3 Experimental procedures

### 3.1 Mechanical testing

Reversed loading tests were performed to study the influence of pre-compression on the ductile fracture properties of the alloys. Diabolo-shaped specimens were selected to prevent barrelling and buckling at large compressive strains. The specimens were machined from the centre of the extruded profile, oriented along TD, and had a minimum diameter of 6.4 mm with a notched radius of 3.6 mm. Fig. 2 illustrates the specimen geometry.
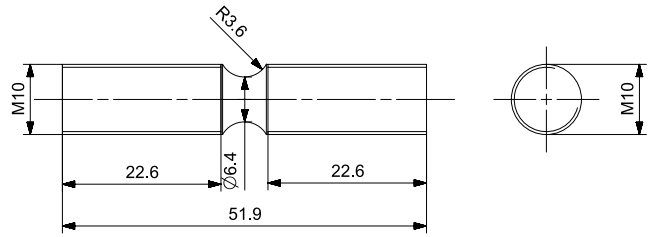
Fig. 2: Geometry of the test specimen

A displacement controlled Zwick testing machine was used with a constant cross-head velocity of 0.50 mm/min. The force and minimum diameter of the specimen in two orthogonal directions were continuously measured during the test until fracture. An in-house measuring system with two orthogonal lasers was used to measure the minimum diameters in the extrusion direction (ED) and thickness direction (ND) of the specimen. The system consists of a high-speed, contact-less AEROEL XLS13XY laser gauge with 1 $\mu$m resolution, mounted on a mobile frame. Operation of the mobile frame ensured that the diameters at the minimum cross-section were measured during the test. The setup of the tests is presented in Fig. 3. Special connectors were used to fasten the specimen in the testing machine to ensure a smooth transition from compression to tension loading.

Assuming an elliptical shape of the deformed cross-section, one can calculate the current cross-sectional area as

$$A = \frac{\pi}{4} D_1 D_2 \tag{1}$$

Fig. 1: Equivalent stress versus equivalent plastic strain curves for the three alloys (AA6060 and AA6082.25 from Khadyko et al. 2014)
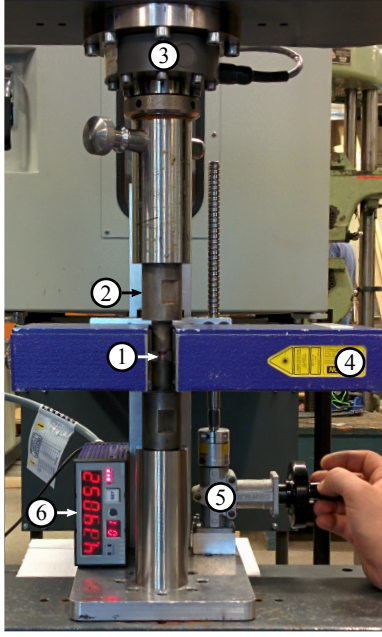
Fig. 3: Setup of the reversed loading tests: ① specimen, ② connector, ③ load cell, ④ laser micrometer, ⑤ vertical adjustment, ⑥ display connected to the computer

where $D_1$ and $D_2$ are the measured diameters in ED and ND, respectively. The true stress can be expressed as

$$\sigma = \frac{F}{A} \qquad (2)$$

where $F$ is the measured force. Also assuming plastic incompressibility and negligible elastic strains, the logarithmic strain can be calculated as

$$\varepsilon = \ln\left(\frac{A_0}{A}\right) \qquad (3)$$

where $A_0 = \frac{\pi}{4}D_0^2$ is the initial cross-sectional area and $D_0$ is the measured initial minimum diameter. Note that the calculated true stress and logarithmic strain measured are average values over the minimum cross-section of the specimen.

For each alloy 15 specimens were tested in three series (series 1, 2 and 3) with five different levels of pre-compression. These specimens were first compressed to a predefined strain level (0%, 10%, 20%, 30% and 40% pre-compression) and then pulled to fracture in tension. To study the microstructure at different stages during the reversed loading, four, five and six additional specimens (series 4) were tested for the AA6060, AA6082.25 and AA6082.50 alloys, respectively. Four specimens for each alloy in test series 4 were successfully completed. These specimens were subjected to 0%, 10% and 40% pre-compression. Three samples were stopped and unloaded close to failure in tension, while the last specimen was subjected to 40% compression and unloaded. A summary of the tests carried out is presented in Table 2.

### 3.2 Microstructure characterisation

Samples from the three alloys were mechanically ground and polished. Back scattered electron (BSE) micrographs of the samples, showing the constituent particles, were taken in a Hitachi SU-6600 FESEM operated at 5.0 kV. To reveal the grain structure under polarised light in the optical microscope, the samples were anodised at room temperature for two minutes using $HBF_4$.

The electron back-scatter diffraction (EBSD) technique was used to obtain the crystallographic texture, operating the Hitachi SU-6600 FESEM at 20 kV. The EBSD measurements were carried out in the ED-ND plane for the AA6060 and AA6082.25 alloys and in the ND-TD plane for the AA6082.50 alloy, due to the shape of the large elongated grains, using a step size of 10 $\mu$m, 5 $\mu$m and 8 $\mu$m, respectively. A total of 2611, 25512 and 1565 grains were measured for the AA6060, AA6082.25 and AA6082.50 alloys, respectively. The orientation distribution functions (ODF) were calculated using a harmonic series expansion and orthotropic sample symmetry with a series rank of 23 and Gaussian smoothing of 7°.

Fracture surfaces of the failed specimens were investigated in a Zeiss Gemini Supra 55 VP FESEM operated at 10 kV. A selection of the fractured specimens (series 1, 2 and 3) and the specimens stopped during the reversed loading (series 4) were sliced along the ND-TD plane, i.e., along the specimen axis, and the sliced surface was polished and investigated in the scanning electron microscope (SEM) to unveil the fracture mechanisms. In addition, the sliced surface was polished and anodised to study the grain structure after fracture in an optical microscope.

The specimens of test series 4 were further ion-milled at 4kV for 5 min with a 85° tilt. This was done to remove any excess material that might have been polished into any of the possible voids present on the polished surface.

## 4 Results

### 4.1 Initial microstructure

The grain structure of the three alloys is presented in Fig. 4. The AA6060 alloy has a recrystallized, equi-axed grain structure with a grain size of approximately 60-70 $\mu$m. In contrast, the AA6082.25 alloy exhibits a typical fibrous, non-recrystallized grain structure with grains that are several millimetres long in the ED, about 10 $\mu$m in the ND and about 150 $\mu$m in the TD of the profile. In addition, the fibrous structure comprises sub-grains approximately 2-10 $\mu$m in diameter with low-angle grain boundaries. The AA6082.50 alloy has a recrystallized grain structure with large elongated grains that are about 300-400 $\mu$m wide and several millimetres long.

Table 2: Test matrix

| Pre-compression | Test number | | | | | |
| | Series 1 | Series 2 | Series 3 | Series 4 | | |
| | | All alloys | | AA6060 | AA6082.25 | AA6082.50 |
| 0% | 1 | 2 | 3 | 16 | 16,17 | 16,17 |
| 10% | 4 | 5 | 6 | 17 | 18 | 18 |
| 20% | 7 | 8 | 9 | - | - | - |
| 30% | 10 | 11 | 12 | - | - | - |
| 40% | 13 | 14 | 15 | 18,19 | 19,20 | 19,20,21 |
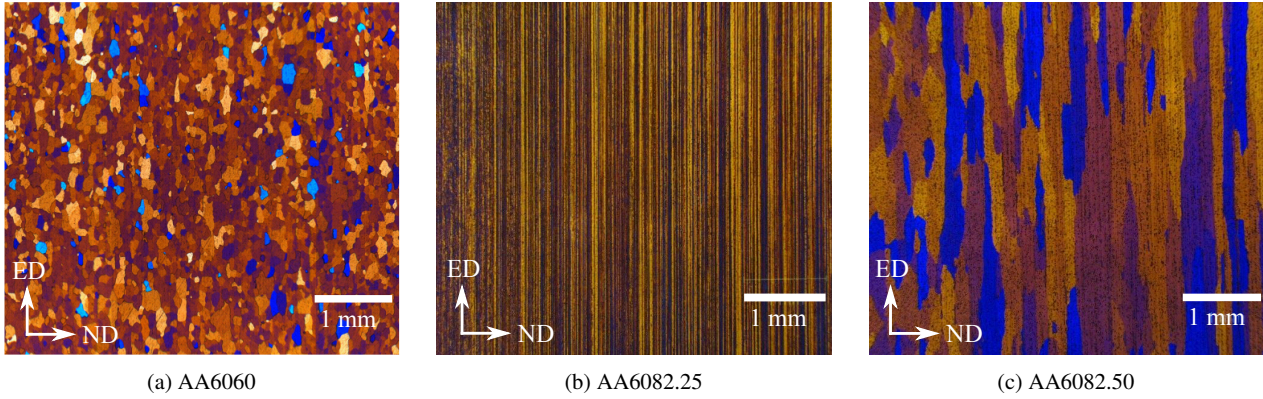


(a) AA6060  (b) AA6082.25  (c) AA6082.50

Fig. 4: Grain structure of the three alloys (AA6060 and AA6082.25 from Khadyko et al. 2014)
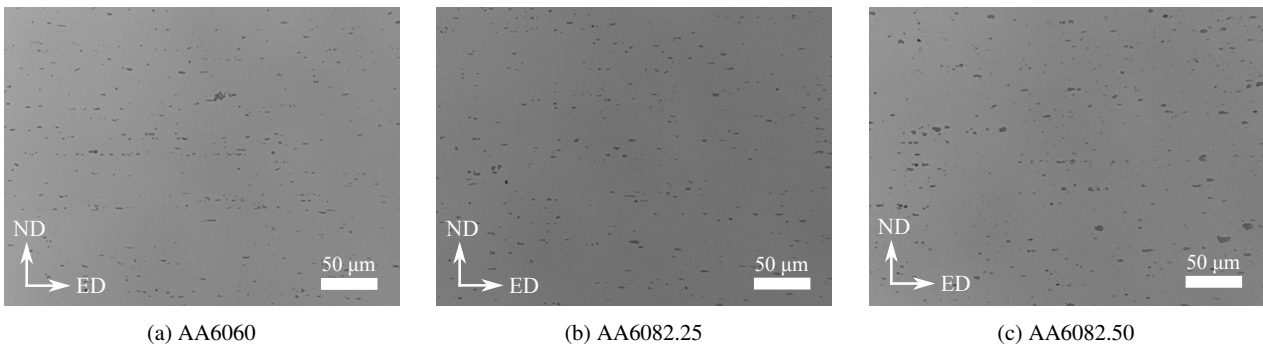


(a) AA6060  (b) AA6082.25  (c) AA6082.50

Fig. 5: Distribution of constituent particles in the three alloys

Fig. 5 illustrates the size and distribution of the constituent particles. These particles are lined up in stringers along the ED, and the distribution is reasonably similar for the three alloys. The measured area fraction of particles is $f_p = 0.0093$, $f_p = 0.0120$ and $f_p = 0.0139$ for the AA6060, AA6082.25 and AA6082.50 alloys, respectively.

The crystallographic texture of the alloys is presented as ODFs in Fig. 6. A strong cube texture with a minor Goss component is observed for the AA6060 alloy. The AA6082.25 alloy exhibits a cube texture with orientations along the $\beta$-fibre, which goes from the copper to the brass orientation, through the S component. For the AA6082.50 alloy, a rotated cube texture is observed, with an approximate 45° rotation about the ND.

The grain structure and crystallographic texture of the AA6060 and AA6082.25 alloys were obtained by Khadyko et al. (2014).

4.2 Stress-strain response

True stress and logarithmic strain were calculated from the force and diameter measurements for the reversed loading tests, see Eqs. 1-3, and the resulting stress-strain curves are presented in Fig. 7.

The Bauschinger effect is observed after load reversal and reaches its maximum at around 10% pre-compression. For larger pre-compression levels, the Bauschinger effect gradi-
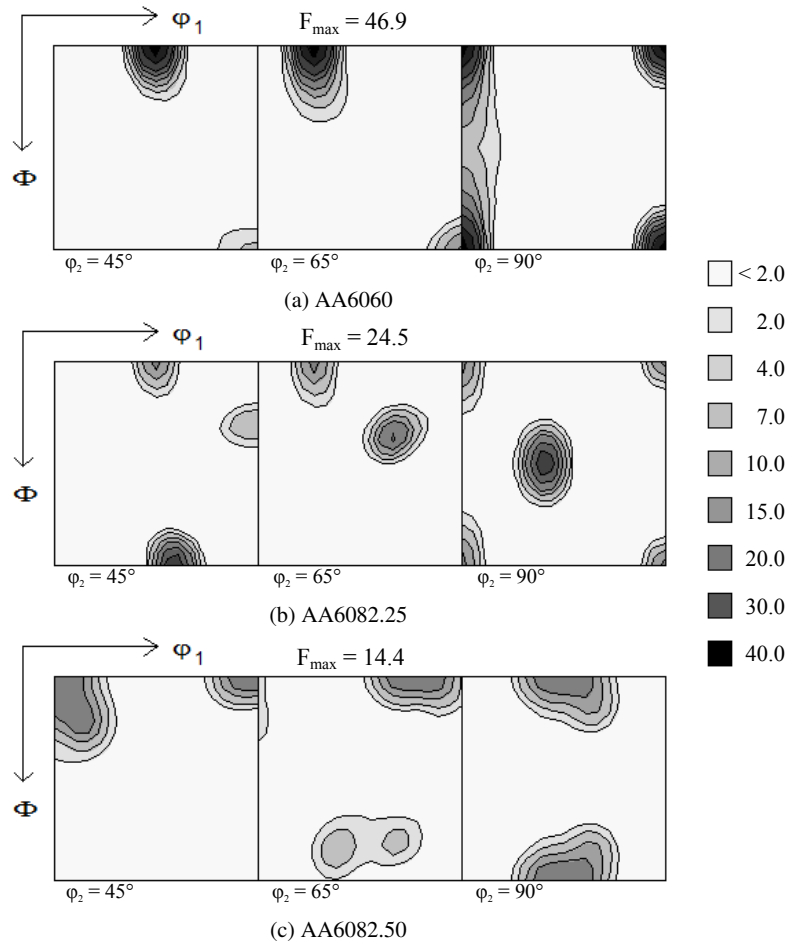
Fig. 6: Orientation distribution functions for the three alloys, showing sections for $\varphi_2 = 45°$, $65°$ and $90°$

ally decreases for all three alloys. Note that the Bauschinger effect is amplified by the triaxial stress field in the notched area of the specimen.

Another noticeable feature is that the initial yield stress and the flow stress at small plastic strains are higher in compression than in tension, i.e., the three alloys exhibit the strength differential (SD) effect. The SD effect has also been observed by others, e.g., Spitzig and Richmond (1984); Wilson (2002); Bai and Wierzbicki (2008). The physical origin of the SD effect has not been established for the present materials, but Spitzig and Richmond (1984) suggested that it is linked to the effect of hydrostatic pressure on dislocation motion.

The yield stress at 0.2% plastic strain in tension and compression as well as the re-yielding stress at 0.2% plastic strain after load reversal are given in Table 3 for the three alloys. The re-yielding stresses are lower than the initial yield stress due to the Bauschinger effect. For the AA6060 and the AA6082.50 alloys, the re-yielding stress increases with increasing pre-compression, while for the AA6082.25

alloy the re-yielding stress is almost independent of pre-compression.

The measured Lankford coefficients, giving the ratio between the incremental strain in ED and ND, for pure tension, compression and in tension after pre-compression are given in Table 4. The Lankford coefficients are different in tension and compression, and between the alloys. Accordingly, the cross-section of the specimens evolve differently for each alloy. Note that since the calculated logarithmic strains are average values over the cross-section of the specimen, locally the strains could be significantly different between the alloys due to differences in the cross-section geometry. Only small differences are seen in the Lankford coefficients in tension after pre-compression to different levels.

It is seen in Fig. 7 that the AA6082.25 alloy exhibits softening at relatively large compressive strains. As the compression increases beyond approximately 20%, the magnitude of the true stress decreases for the AA6082.25 alloy, whereas the magnitude of the true stress increases monotonically with increasing compression for the AA6060 and AA6082.50 alloys. This softening is related to the grain structure of this

(a) AA6060
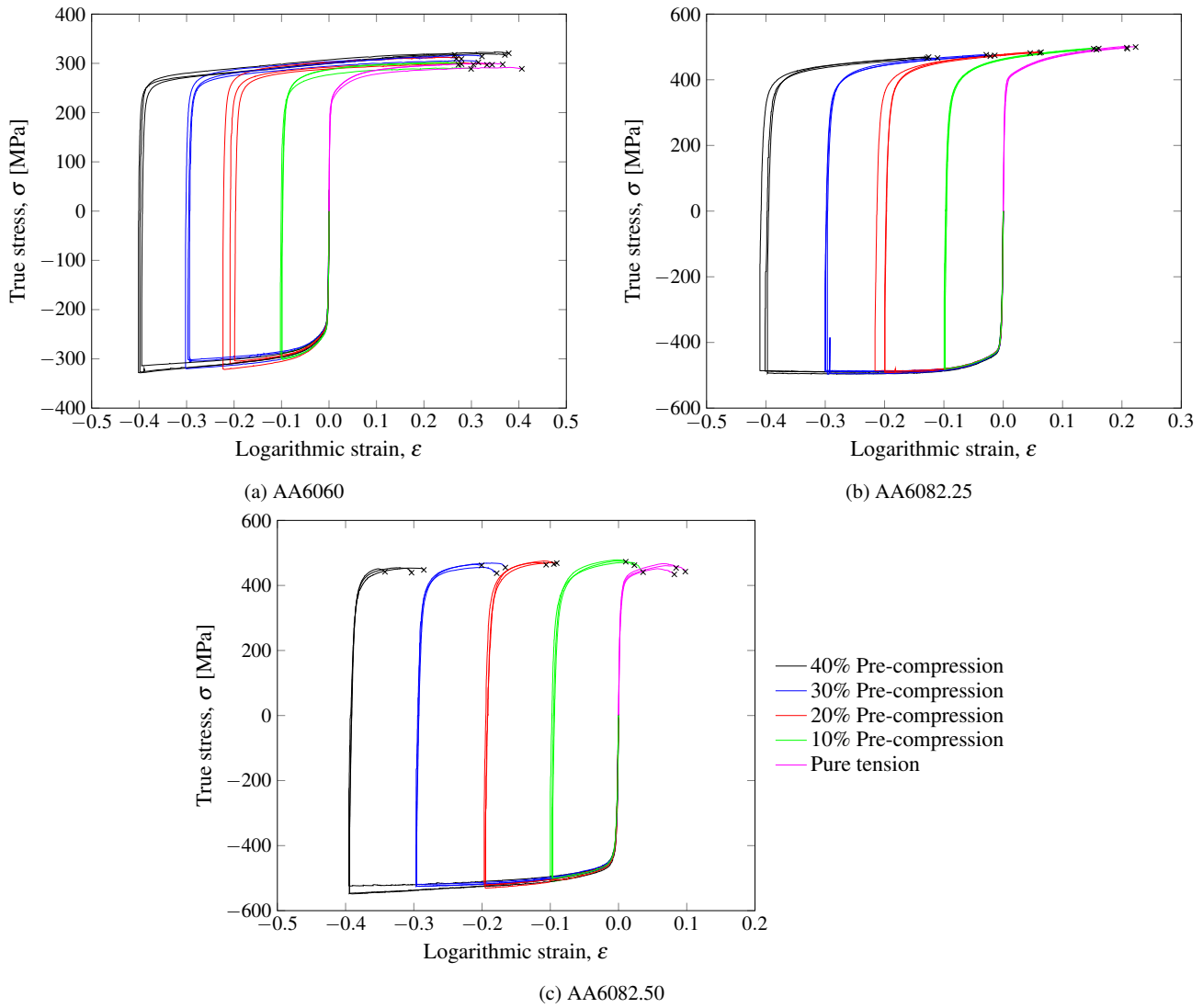
(b) AA6082.25

(c) AA6082.50

Fig. 7: True stress versus logarithmic strain curves for the three alloys to failure from test series 1, 2 and 3. The point of failure is indicated with a cross

Table 3: Yield stresses at 0.2% plastic strain, $\sigma_{0.2}$, and re-yielding stresses after pre-compression, with standard deviations

| Alloy | Tension | Compression | Re-yielding after 10% pre-compression | Re-yielding after 20% pre-compression | Re-yielding after 30% pre-compression | Re-yielding after 40% pre-compression |
|---|---|---|---|---|---|---|
| AA6060 | $207.0 \pm 4.7$ MPa | $-221.4 \pm 5.8$ MPa | $184.7 \pm 5.6$ MPa | $187.6 \pm 9.2$ MPa | $195.4 \pm 5.5$ MPa | $201.8 \pm 4.3$ MPa |
| AA6082.25 | $362.7 \pm 10.2$ MPa | $-381.6 \pm 7.0$ MPa | $272.9 \pm 3.5$ MPa | $269.2 \pm 6.4$ MPa | $269.6 \pm 3.9$ MPa | $269.1 \pm 6.1$ MPa |
| AA6082.50 | $356.3 \pm 13.5$ MPa | $-391.6 \pm 8.9$ MPa | $283.7 \pm 1.2$ MPa | $305.1 \pm 2.8$ MPa | $315.1 \pm 5.7$ MPa | $315.8 \pm 8.1$ MPa |

Table 4: Measured Lankford coefficients in tension, compression and in tension after pre-compression, with standard deviations

| Alloy | Tension | Compression | In tension after 10% pre-compression | In tension after 20% pre-compression | In tension after 30% pre-compression | In tension after 40% pre-compression |
|---|---|---|---|---|---|---|
| AA6060 | $1.27 \pm 0.01$ | $1.36 \pm 0.10$ | $1.35 \pm 0.01$ | $1.37 \pm 0.04$ | $1.43 \pm 0.05$ | $1.50 \pm 0.13$ |
| AA6082.25 | $0.97 \pm 0.01$ | $0.95 \pm 0.02$ | $0.96 \pm 0.01$ | $0.94 \pm 0.01$ | $0.93 \pm 0.00$ | $0.91 \pm 0.01$ |
| AA6082.50 | $0.36 \pm 0.05$ | $0.55 \pm 0.05$ | $0.45 \pm 0.04$ | $0.45 \pm 0.05$ | $0.38 \pm 0.05$ | $0.42 \pm 0.08$ |

alloy, as the thin, elongated grains, seen in Fig. 4b, are more eligible to "internal buckling" in compression under the superimposed multiaxial stress state, see Section 4.5.

Fig. 7 shows that the response after pre-compression also vary among the alloys. For the AA6060 alloy, the point of failure occurs within a narrow range of strain values, i.e., the failure strain is almost independent of pre-compression. Conversely, the point of failure of the AA6082.25 and AA6082.50 alloys is clearly dependent of pre-compression. The AA6060 alloy does not exhibit a marked drop in load level at failure, instead the load decreases steadily towards zero. Therefore, the point of failure for the AA6060 alloy is defined as the point where a distinct change in the slope of the true stress versus logarithmic strain curve is observed. For the AA6082.25 and AA6082.50 alloys, the point of failure is defined as the point where a marked drop in the load level occurs. The point of failure is indicated with a cross in Fig. 7.

### 4.3 Effect of pre-compression on the ductility

As shown in Fig. 7, the point of failure for the AA6060 alloy occurred within a narrow range of strain values for different levels of pre-compression, while the strain at failure decreased for the AA6082.25 and AA6082.50 alloys with increasing pre-compression. Fig. 8 presents the influence of pre-compression on the failure strain and the relative failure strain. The relative failure strain is here defined as the strain to failure measured with respect to the compressed configuration. Hence, the strain to failure is given by $\varepsilon_f = \ln(A_0/A_f)$, where $A_f$ is the measured cross-sectional area at failure, and the relative failure strain is defined as $\varepsilon_r = \varepsilon_f - \varepsilon_0 = \ln(A_r/A_f)$, where $\varepsilon_0 = \ln(A_0/A_r)$ is the measured strain and $A_r$ the measured cross-sectional area at load reversal. Note that due to the change of the specimen geometry after pre-compression, the stress triaxiality in the specimen will change, and probably influence the point of failure. As a result, the measured failure strains will depend to some extent on geometrical effects as well as load reversal effects.

From Fig. 8 one can see that pre-compression has a significant influence on the ductility of the aluminium alloys. For the AA6060 alloy, the failure strain is approximately constant with respect to pre-compression, resulting in a marked increase in the relative failure strain and the ductility of the alloy. Note that here we define ductility as the deformation capability of the material subsequent to the pre-deformation. For a pre-compression of 40%, the relative failure strain is approximately doubled with respect to the case of pure tension. A decrease in the failure strain is observed for the AA6082.25 alloy, but the relative failure strain and thus the ductility of the alloy increases with increasing pre-compression. However, the increase in the relative failure strain is not nearly as large for the AA6082.25 alloy as for the AA6060 alloy. The failure

strain of the AA6082.50 alloy decreases with increasing pre-compression, and the decrease is approximately equal to the level of pre-compression. This results in an approximately constant relative failure strain, and, accordingly, the ductility of the alloy is almost independent of pre-compression. In Fig. 7c, one can observe this by the tension part of the true stress-logarithmic strain curves after pre-compression being reasonably similar for all the levels of pre-compression tested.

The data visualized in Fig. 8 together with the true stress at failure $\sigma_f$ and the maximum true stress $\sigma_{max}$ are given in Tables 5, 6 and 7 for the AA6060, AA6082.25 and AA6082.50 alloys, respectively. Both $\sigma_f$ and $\sigma_{max}$ increase with increasing pre-compression for the AA6060 alloy and decrease for the AA6082.25 alloy. For the AA6082.50 alloy, $\sigma_f$ and $\sigma_{max}$ increase from 0% pre-compression to approximately 20% and then start to decrease.

### 4.4 Fracture investigation

To get a deeper understanding of the mechanisms involved during the reversed loading process, a fractographic analysis of the tested specimens was performed. Fig. 9 presents the fracture surfaces for the three alloys subjected to pure tension (0% pre-compression) and 40% pre-compression. The three alloys exhibit different fracture surfaces. The AA6060 alloy displays cup-and-cone fracture, indicating that fracture initiates at the centre and grows outwards. The fracture surface has a diamond shaped cross-sectional area. Also the AA6082.25 alloy exhibits cup-and-cone fracture but the fracture surface is circular, consisting of a flat middle section and shear lips towards the edge. In contrast, the AA6082.50 alloy displays a shear failure mode which is a result of the large grains. Dark lines crossing the fracture surface indicate intercrystalline fracture along grain boundaries.

With increasing pre-compression the fracture surfaces change, and for 40% pre-compression the fracture surface of the AA6060 alloy is more elliptical than the clear diamond shape observed for pure tension. The fracture surface of the AA6082.25 alloy subjected to 40% pre-compression is similar, but the fracture area is larger than for pure tension, indicating a lower fracture strain. The shear fracture mode observed for the AA6082.50 alloy becomes stronger with increasing pre-compression, and the cross-sectional area is also larger and more elliptical than for pure tension.

Fig. 10 presents the fracture surfaces with a higher magnification in the centre of the specimens shown in Fig. 9. Primary particles can be seen in the bottom of the many dimples indicating ductile fracture involving nucleation, growth and coalescence of voids. Even though particles are not observed in the bottom of all the dimples one can not exclude the presence of them. Particles may be present in the opposite
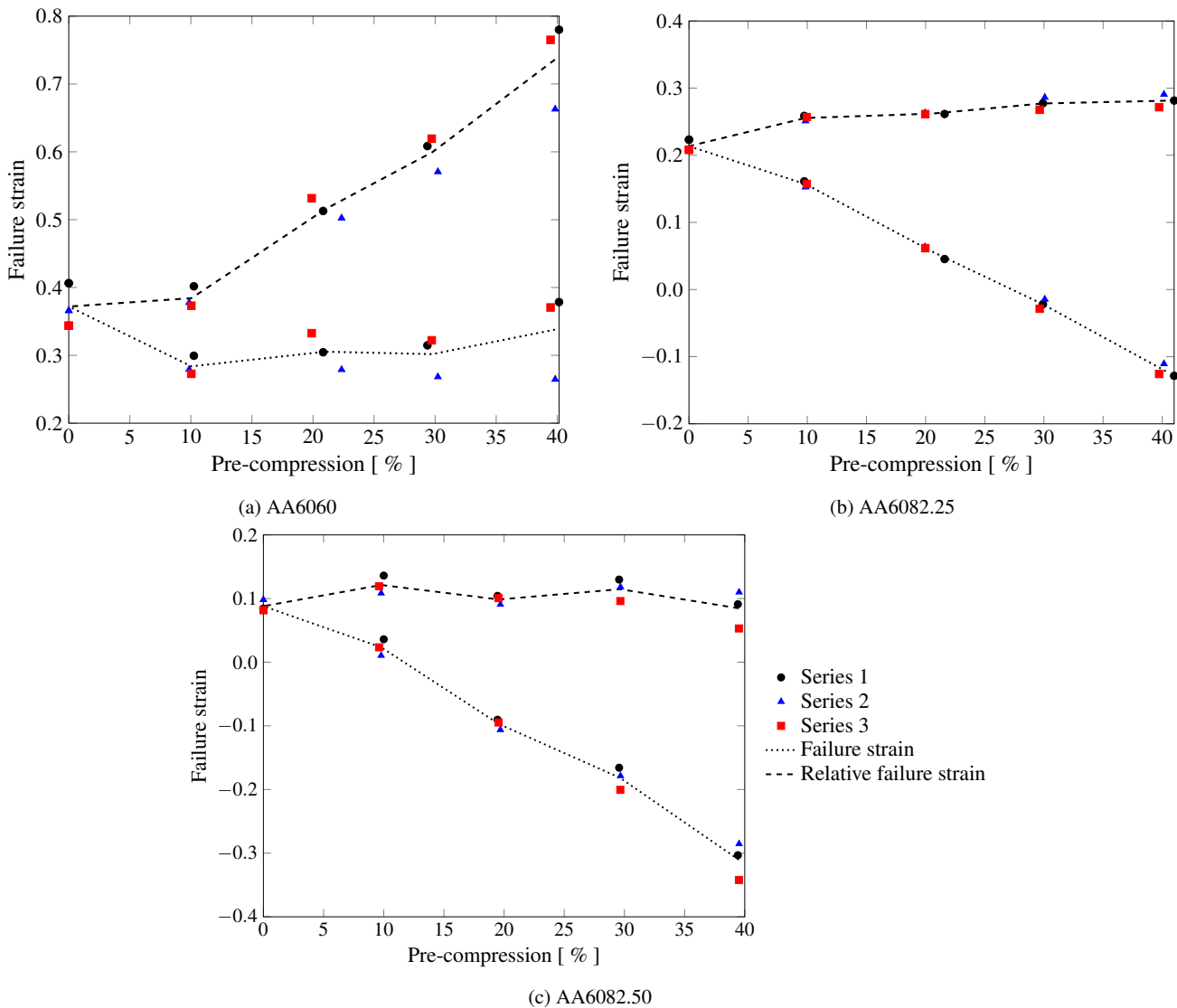
(a) AA6060

(b) AA6082.25

(c) AA6082.50

Fig. 8: Failure strain and relative failure strain versus pre-compression level for the three alloys based on test series 1, 2 and 3. The failure strain and the relative failure strain are as given in Tables 5, 6 and 7. The relative failure strain is the strain to failure measured with respect to the compressed configuration

fracture surface or have fallen out during preparation. Studying the dimples and the particles more closely, see Fig. 11, one can observe cracked particles in some of the dimples. As a result, voids may have been nucleated from primary particles either by decohesion or by particle cracking (Maire et al. 2011), or the voids may have been pre-existing in the material (Campbell 2011; Toda et al. 2013) prior to the reversed loading. A combination of these mechanisms is probably in operation. This will further be investigated in Section 4.5.

Different dimple structures are observed on the fracture surfaces of the three alloys and for the specimens subjected to different levels of pre-compression. The dimples observed can be categorised into two main categories, i.e., a low density of coarse dimples and a high density of fine dimples.

These fine dimples, without particles, indicate that also other mechanisms are involved, e.g. voids may be created in the junction points of interacting slip planes (Pedersen et al. 2008).

For the specimens subjected to pure tension, fracture is mainly transcrystalline for all three alloys, however some areas of intercrystalline fracture are observed. The fracture surfaces of the AA6060 and AA6082.25 alloys pre-compressed to 40% are also mainly comprised of transcrystalline fracture as in the samples subjected to pure tension. The fracture surface of the AA6060 alloy subjected to 40% pre-compression has fewer areas of intercrystalline fracture than the one subjected to pure tension, while for the AA6082.25 alloy no difference is found. In contrast, the fracture surface of the

Table 5: Results from test series 1, 2 and 3 for the AA6060 alloy

| Test № | Pre-strain $\varepsilon_0$ | Failure strain $\varepsilon_f$ | Relative failure strain $\varepsilon_r = \varepsilon_f - \varepsilon_0$ | Failure stress $\sigma_f$ [MPa] | Max true stress $\sigma_{max}$ [MPa] |
|---|---|---|---|---|---|
| 1 | 0.000 | 0.406 | 0.406 | 288.9 | 292.0 |
| 2 | 0.000 | 0.366 | 0.366 | 298.0 | 300.6 |
| 3 | 0.000 | 0.344 | 0.344 | 297.1 | 300.0 |
| 4 | -0.102 | 0.299 | 0.401 | 288.7 | 290.9 |
| 5 | -0.099 | 0.279 | 0.378 | 298.4 | 302.1 |
| 6 | -0.100 | 0.273 | 0.373 | 297.2 | 300.6 |
| 7 | -0.208 | 0.305 | 0.513 | 297.5 | 301.3 |
| 8 | -0.223 | 0.279 | 0.502 | 309.0 | 312.5 |
| 9 | -0.199 | 0.333 | 0.532 | 296.9 | 299.9 |
| 10 | -0.294 | 0.315 | 0.609 | 302.0 | 305.9 |
| 11 | -0.302 | 0.268 | 0.570 | 309.4 | 312.7 |
| 12 | -0.297 | 0.322 | 0.619 | 314.0 | 317.0 |
| 13 | -0.401 | 0.379 | 0.780 | 320.5 | 322.9 |
| 14 | -0.398 | 0.265 | 0.663 | 317.3 | 319.4 |
| 15 | -0.395 | 0.371 | 0.766 | 317.1 | 319.6 |

Table 6: Results from test series 1, 2 and 3 for the AA6082.25 alloy

| Test № | Pre-strain $\varepsilon_0$ | Failure strain $\varepsilon_f$ | Relative failure strain $\varepsilon_r = \varepsilon_f - \varepsilon_0$ | Failure stress $\sigma_f$ [MPa] | Max true stress $\sigma_{max}$ [MPa] |
|---|---|---|---|---|---|
| 1 | 0.000 | 0.223 | 0.223 | 499.7 | 501.1 |
| 2 | 0.000 | 0.209 | 0.209 | 494.8 | 496.8 |
| 3 | 0.000 | 0.208 | 0.208 | 497.8 | 501.7 |
| 4 | -0.097 | 0.161 | 0.258 | 495.1 | 496.5 |
| 5 | -0.098 | 0.153 | 0.251 | 494.5 | 496.3 |
| 6 | -0.100 | 0.157 | 0.257 | 491.8 | 493.2 |
| 7 | -0.216 | 0.045 | 0.261 | 481.4 | 483.2 |
| 8 | -0.200 | 0.064 | 0.264 | 484.0 | 485.6 |
| 9 | -0.200 | 0.062 | 0.262 | 482.0 | 482.8 |
| 10 | -0.299 | -0.022 | 0.277 | 471.9 | 474.8 |
| 11 | -0.301 | -0.015 | 0.286 | 474.1 | 474.4 |
| 12 | -0.296 | -0.029 | 0.267 | 476.1 | 476.7 |
| 13 | -0.410 | -0.129 | 0.281 | 465.5 | 468.7 |
| 14 | -0.401 | -0.111 | 0.290 | 466.5 | 466.9 |
| 15 | -0.397 | -0.126 | 0.271 | 469.1 | 469.6 |

Table 7: Results from test series 1, 2 and 3 for the AA6082.50 alloy

| Test № | Pre-strain $\varepsilon_0$ | Failure strain $\varepsilon_f$ | Relative failure strain $\varepsilon_r = \varepsilon_f - \varepsilon_0$ | Failure stress $\sigma_f$ [MPa] | Max true stress $\sigma_{max}$ [MPa] |
|---|---|---|---|---|---|
| 1 | 0.000 | 0.084 | 0.084 | 453.8 | 467.0 |
| 2 | 0.000 | 0.098 | 0.098 | 442.5 | 460.8 |
| 3 | 0.000 | 0.082 | 0.082 | 433.9 | 451.6 |
| 4 | -0.100 | 0.036 | 0.136 | 440.7 | 471.4 |
| 5 | -0.098 | 0.010 | 0.108 | 472.9 | 478.9 |
| 6 | -0.096 | 0.023 | 0.119 | 462.2 | 475.2 |
| 7 | -0.195 | -0.090 | 0.105 | 468.8 | 470.5 |
| 8 | -0.197 | -0.106 | 0.091 | 463.6 | 470.3 |
| 9 | -0.195 | -0.095 | 0.100 | 465.7 | 475.4 |
| 10 | -0.296 | -0.166 | 0.130 | 455.0 | 469.1 |
| 11 | -0.297 | -0.179 | 0.118 | 437.7 | 456.1 |
| 12 | -0.297 | -0.201 | 0.096 | 461.8 | 465.0 |
| 13 | -0.394 | -0.303 | 0.091 | 439.3 | 454.7 |
| 14 | -0.395 | -0.285 | 0.110 | 447.8 | 453.7 |
| 15 | -0.395 | -0.342 | 0.053 | 441.9 | 451.3 |

(a) AA6060 - 0% pre-compression

(b) AA6060 - 40% pre-compression

(c) AA6082.25 - 0% pre-compression

(d) AA6082.25 - 40% pre-compression

(e) AA6082.50 - 0% pre-compression
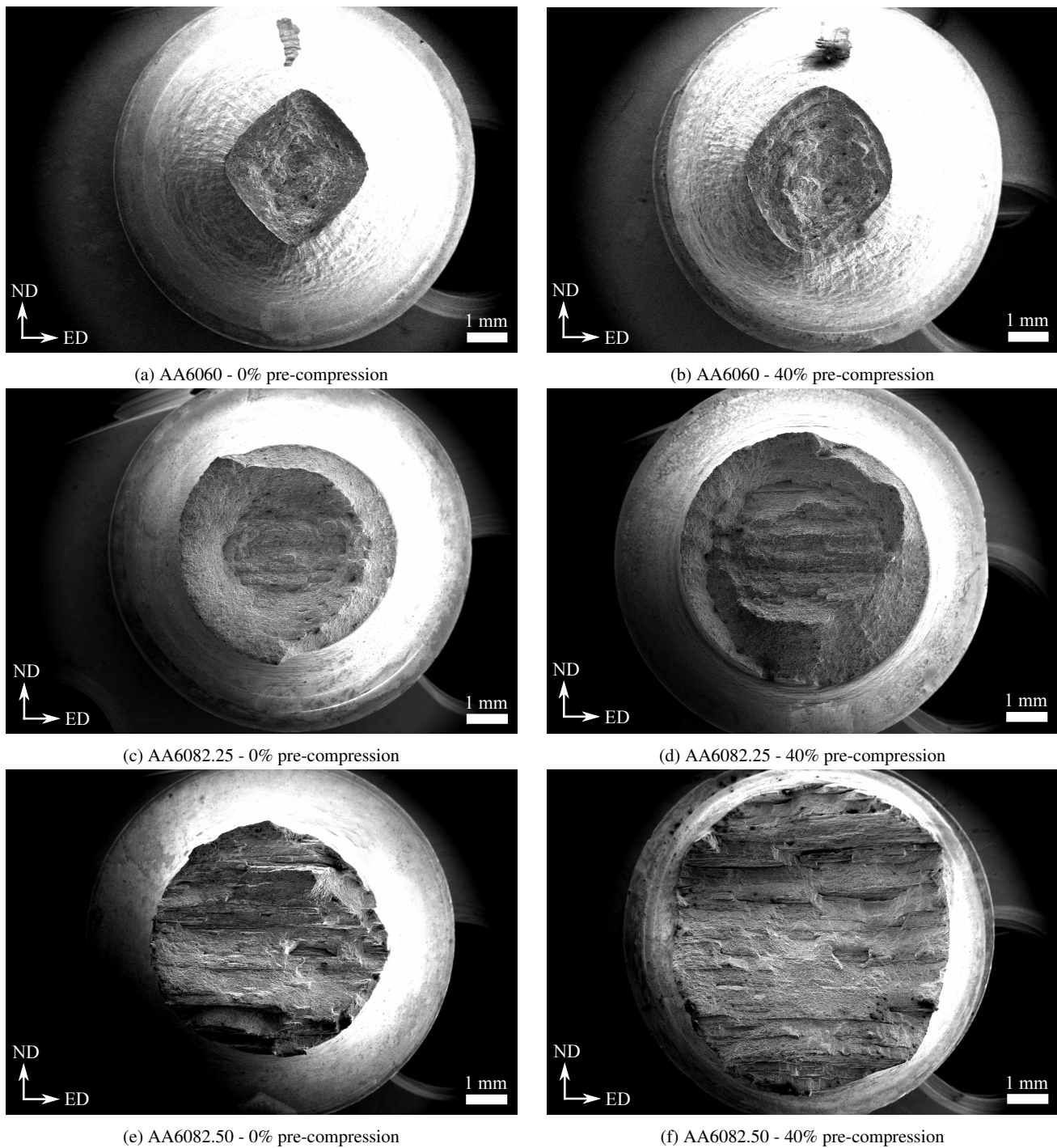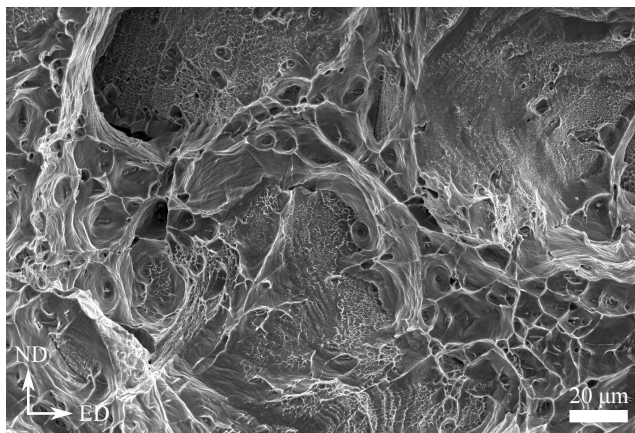
(f) AA6082.50 - 40% pre-compression

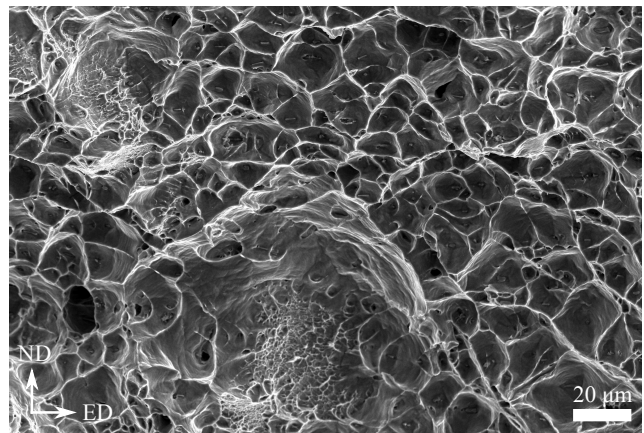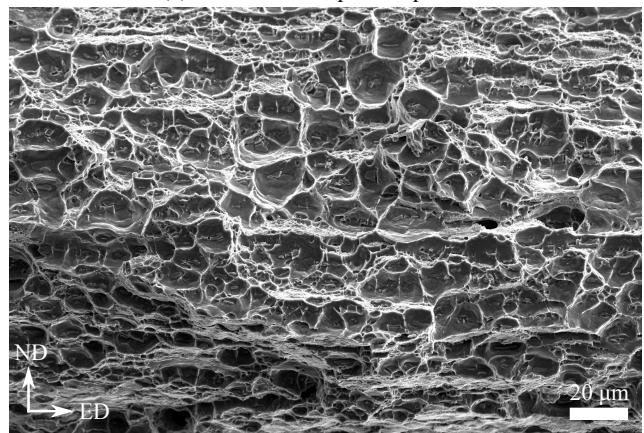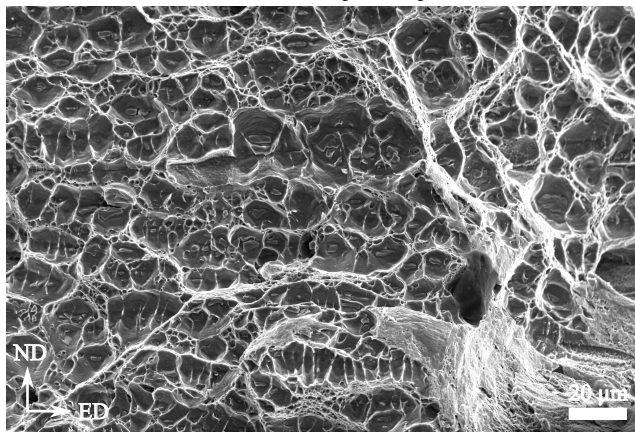Fig. 9: Fracture surfaces for the three alloys: pure tension, test №1, (left) and 40% pre-compression, test №13 (right)

AA6082.50 alloy subjected to 40% pre-compression has fewer areas with large dimples, and the dimples are smeared out over the fracture surface.

Studying the dimples more closely one can see that the depth of the dimples varies between the alloys and with different levels of pre-compression; the general trend being that the dimple depth increases with increasing tensile ductil-ity. The deepest dimples are observed for the AA6060 alloy. The AA6082.25 alloy has more shallow dimples and the AA6082.50 has the most shallow dimples of the three alloys. For the AA6060 alloy, the dimples of the specimen subjected to 40% pre-compression are deeper than the dimples observed for the specimen subjected to pure tension. On the contrary, the dimples of the AA6082.25 and the AA6082.50

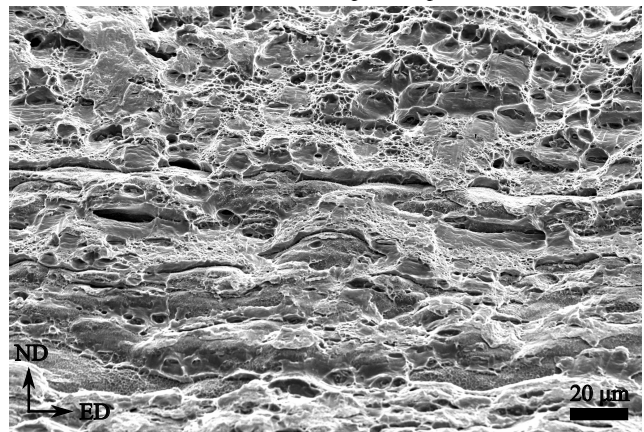(a) AA6060 - 0% pre-compression
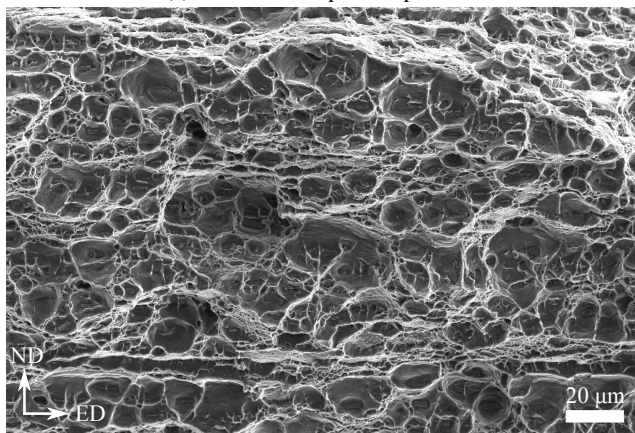


(b) AA6060 - 40% pre-compression



(c) AA6082.25 - 0% pre-compression



(d) AA6082.25 - 40% pre-compression



(e) AA6082.50 - 0% pre-compression



(f) AA6082.50 - 40% pre-compression

Fig. 10: Local fracture surfaces for the three alloys: pure tension, test №1, (left) and 40% pre-compression, test №13 (right)

alloys get more shallow with increasing pre-compression. For the AA6082.25 alloy, this is better seen in Fig. 11, where both the difference in depth and the cracked particles in the bottom of the dimples can be observed. Fig. 11 also reveals small areas of intercrystalline fracture with a high density of smaller dimples. It is reasonable to assume that smaller dimples are caused by void growth within the precipitation free zones (PFZs), possibly nucleated at grain boundary precipitates (Chen et al. 2009).

4.5 Microstructure investigation

Owing to the observed decrease in stress level for the AA6082.25 alloy after approximately 20% compression, seen
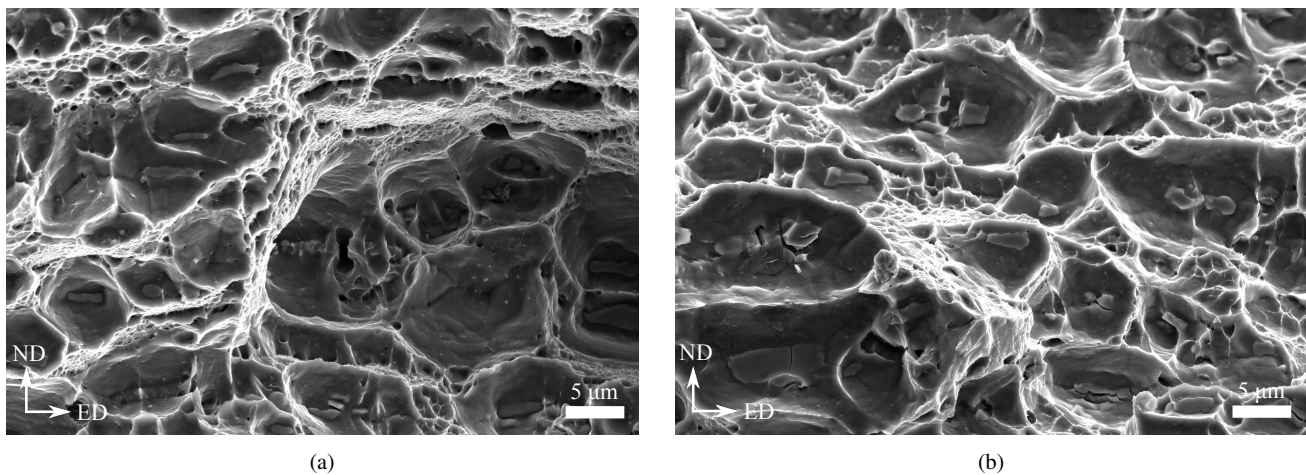
Fig. 11: Local fracture surfaces of the 6082.25 alloy subjected to (a) pure tension and (b) 40% pre-compression
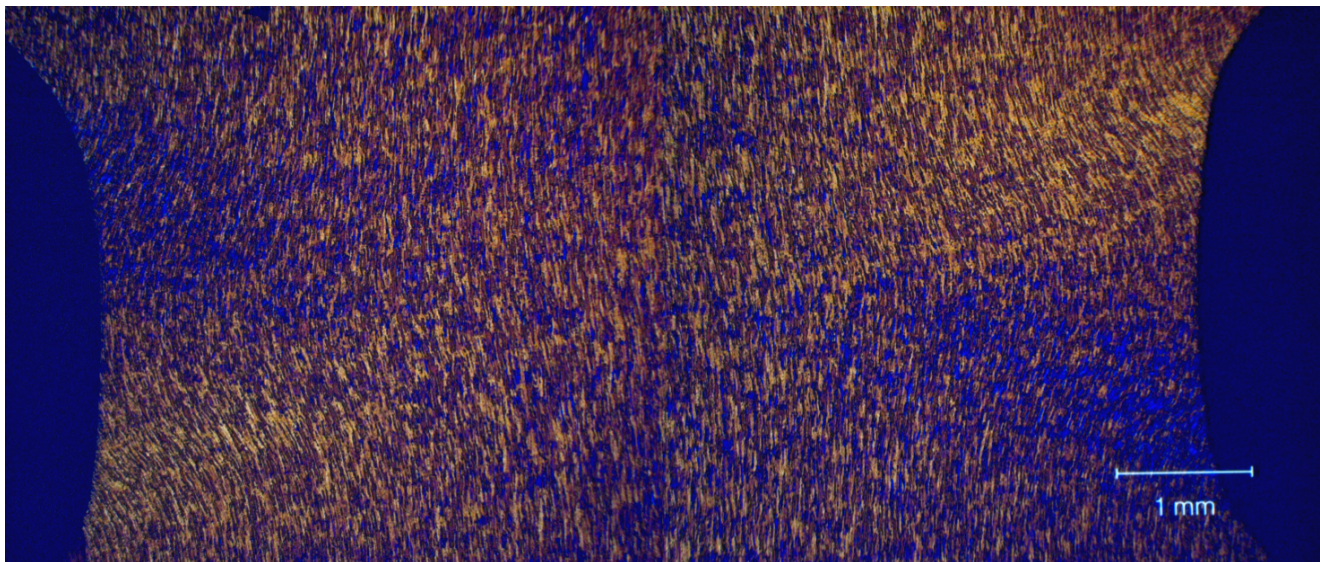


Fig. 12: Deformed grain structure after 40% compression for the AA6082.25 alloy

in Section 4.2, the samples of test series 4 compressed to 40% were investigated in the optical microscope. Fig. 12 presents the deformed grain structure in the notched area for the AA6082.25 alloy. The aligned grain structure, seen initially in Fig. 4b, has been deformed and a wavy grain pattern is observed. In the centre of the specimen, "internal buckling" of the elongated grains is seen, and further towards the periphery the grains are curved and have rotated due to the compression. Crossing shear bands are observed in the notched area extending from the bottom left to the top right (lighter area). This evolution in grain structure is assumed to cause the reduction in stress level observed at large compressive strains. For the AA6060 alloy, the grains are rotated and contains slip bands. The AA6082.50 alloy, having large grains, contains coarse slip bands after deformation.

To investigate the mechanisms involved in the fracture process for these alloys more closely, selected specimens of test series 4 were prepared and investigated in the SEM. Cracked particles can be observed in the samples, see Fig. 13. Fully or partially cracked particles are also found in undeformed samples. These particles have cracked during the extrusion process. It is noted that the particles are larger in the two AA6082 alloys than in the AA6060 alloy. The AA6060 alloy contains constituent particles of type AlFeSi, while the two AA6082 alloys contain constituent particles of type AlFeSiMn. In the samples compressed to 40%, it is difficult to distinguish cracked particles from particles that are not cracked, and therefore the fraction of cracked particles in the alloys could not be determined. There are few visible voids in the samples, which was also the case for the
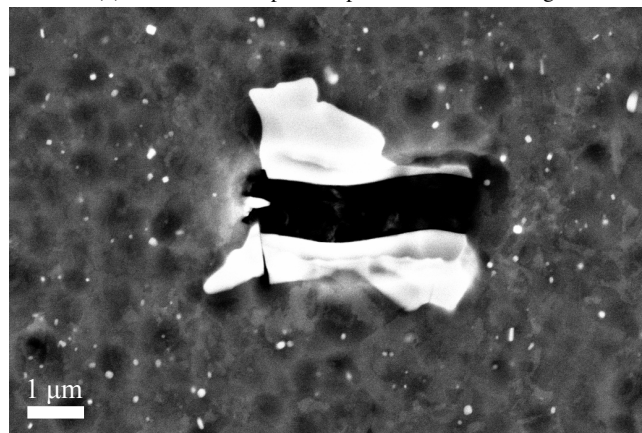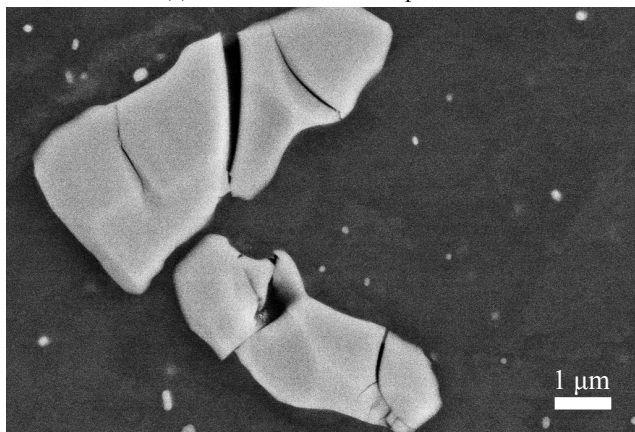
(a) AA6060 - 40% compression
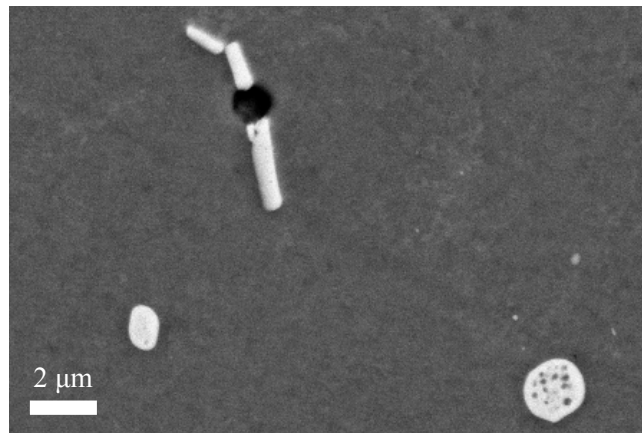
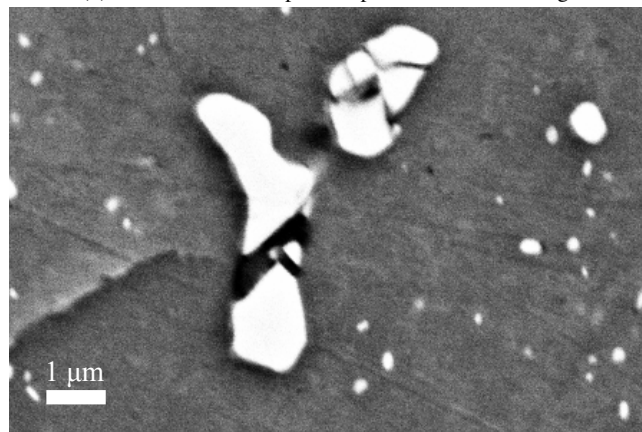(b) AA6060 - 40% pre-compression and stretching
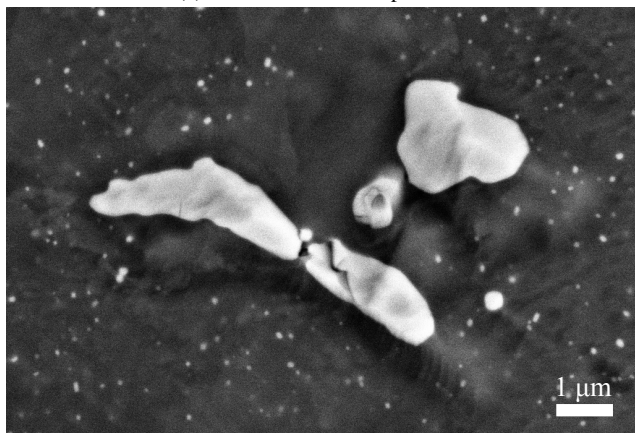
(c) AA6082.25 - 40% compression

(d) AA6082.25 - 40% pre-compression and stretching

(e) AA6082.50 - 40% compression

(f) AA6082.50 - 40% pre-compression and stretching

Fig. 13: Cracked particles in the three alloys after 40% compression (left) and after 40% pre-compression followed by tension and unloading close to failure (right). The loading direction is vertical

undeformed samples. Fig. 13a, c and e display a selection of the observed cracked particles.

After tension a larger number of visible voids are seen, and typically between cracked particles. For the AA6060 alloy, the samples pre-compressed to 40% and stretched display voids formed between cracked particles, see Fig. 13b.

The voids observed to form between cracked particles in the AA6082.25 alloy were in general found to be less developed than those observed for the AA6060 alloy. This indicate that the fracture process is more localised for the AA6082.25 alloy than for the AA6060 alloy, which is reasonable given the markedly higher stress level in the AA6082.25 alloy.

Only small voids are seen between cracked particles in the samples stretched close to failure for the AA6082.50 alloy, and the samples are similar to the one compressed to 40% without stretching. For this alloy, one of the tests pre-compressed to 40% and stretched, was stopped right after a visible crack had developed in the gauge area. Investigating this sample, one can observe cracked particles with voids similar to the AA6082.25 alloy near the crack tip, see Fig. 13f. Hence, the fracture process for both the AA6082.25 and AA6082.50 alloys appears more localised than for the AA6060 alloy. Note that the darker areas visible in Fig. 13d are caused by the ion-milling process.

## 5 Discussion

The tensile ductility of the three alloys without pre-compression was markedly different, see Figs. 1 and 7. The high ductility of the AA6060 alloy compared with the two AA6082 alloys is linked to the large difference in strength. It has been shown in several studies that the tensile ductility of aluminium alloys varies with the yield strength, and for similar microstructure the relation tends to be linear (e.g. Lloyd 2003; Westermann et al. 2014; Pedersen et al. 2015). The difference in tensile ductility between the two AA6082 alloys is explained by the large grains of the AA6082.50 alloy, which was a result of recrystallization and grain growth subsequent to the solution heat treatment. The influence of grain size on the mechanical properties of AlMgSi alloys has been studied by Lohne and Naess (1979). They found that larger grain sizes increased the amount of intercrystalline fracture and reduced the ductility (measured as area reduction at fracture).

The evolution of the relative failure strain, or tensile ductility, with pre-compression level varied between the alloys. While the tensile ductility increased markedly for the AA6060 alloy, it increased slightly for the AA6082.25 alloy and was about constant for the AA6082.50 alloy. A reasonable conjecture which explains the observed difference is that for the lean AA6060 alloy damage is mainly due to growth of existing voids in the vicinity of primary particles (Campbell 2011; Toda et al. 2013), while for the two AA6082 alloys the stress level is sufficiently high to make void nucleation a more favourable mechanism for damage evolution (Pineau et al. 2016).

The fracture surfaces of the aluminium alloys mainly exhibited transcrystalline fracture with some areas of intercrystalline fracture. The PFZ located adjacent to the grain boundaries are assumed to be the cause of intercrystalline fracture (Lohne and Naess 1979). The measured width of the PFZs over high-angle grain boundaries for these alloys, based on transmission electron microscopy (TEM) investigations, is approximately 150 nm and 70 nm for the AA6060 alloy and the two AA6082 alloys, respectively (Christiansen 2017). Crack initiation and growth will occur more easily in the PFZs as the strain will localize in these weaker zones (see e.g. Dowling and Martin 1976; Morgeneyer et al. 2008; Chen et al. 2009; Hoang et al. 2015; Khadyko et al. 2016). The amount of intercrystalline fracture was seen to decrease with increasing pre-compression for the AA6060 alloy, which contributes to the increased tensile ductility of this alloy. A reasonable explanation for this observation is strengthening of the PFZs during compression. Due to the much wider PFZ in the AA6060 alloy, strengthening of the PFZ is deemed to be more favourable for this alloy.

The clear diamond shape observed for the AA6060 alloy is caused by the sharp cube texture combined with the superimposed triaxial stress field. Khadyko et al. (2015) accounted for the strong cube texture of an extruded and naturally aged AA6060 alloy. They performed crystal plasticity finite element simulations of notched tension tests, and obtained a similar diamond-shaped cross-section at large deformations.

Since the area calculations are based on an elliptical shape of the minimum cross-section area (see Section 3.1), the diamond shape observed for the AA6060 alloy will introduce uncertainties in the calculated area at large strains. Based on the crystal plasticity finite element simulations performed by Khadyko et al. (2015), the error is estimated to be at most 10% at failure.

The texture of the alloys will evolve and change during compression. Preliminary crystal plasticity finite element simulations indicate that the cube texture component of the AA6060 and AA6082.25 alloys weakens during compression. Conversely, the rotated cube texture seen for the AA6082.50 alloy strengthens during compression. The weaker cube texture, together with the deformation of the notch geometry, i.e., a lower curvature of the notch after pre-compression, will contribute to the change from a diamond to a more oval shaped fracture surface for the AA6060 alloy, seen in Fig. 9. Albeit the anisotropic deformation is significantly different for the alloys, the main failure mechanisms appear to be similar.

## 6 Concluding remarks

The influence of pre-compression on the ductility of three aluminium alloys heat-treated to peak strength (T6 temper) was studied by conducting reversed loading experiments on diabolo specimens machined from extruded profiles. The three aluminium alloys, AA6060, AA6082.25 and AA6082.50, had different grain structure, grain size and texture. A laser-based measuring system was used to continuously measure the diameters in the extrusion and thickness directions, allowing for the calculation of the logarithmic strain to fracture. Three series with five different levels of pre-compression were conducted, in which the specimens were first compressed to a predefined strain value and then pulled in tension to fracture.

It was found that the failure strain for the AA6060 alloy was almost constant for different levels of pre-compression. Using the compressed configuration as the reference configuration the relative failure strain was observed to increase, resulting in an increased tensile ductility for increasing pre-compression, and for 40% pre-compression the tensile ductility of the AA6060 alloy was approximately doubled compared to pure tension. For the two other alloys, the failure strain was seen to depend on the level of pre-compression, resulting in a decrease in the failure strain for increasing pre-compression. The AA6082.25 alloy had a slight increase in tensile ductility for increasing pre-compression, whereas the AA6082.50 alloy had an approximately constant tensile ductility for the levels of pre-compression tested.

It is concluded that pre-compression has a marked influence on the tensile ductility of the aluminium alloys, and this influence depends on both the microstructure and the strength of the alloy.

The physical mechanisms governing the tensile ductility after pre-compression to various levels have not been established in this study. To further investigate the influence of the stress level, additional reversed loading experiments are planned on two other tempers of the three alloys, namely temper O (annealed) and temper T7 (overaged). In addition, further work will focus on simulations of the reversed loading experiments using crystal plasticity finite element methods, anisotropic metal plasticity and unit cell computations. The numerical study will give insight into the texture development during the loading sequence, the stress and strain distribution over the minimum cross-section area of the specimen and the damage evolution in these anisotropic alloys.

# References

Bai Y, Wierzbicki T (2008) A new model of metal plasticity and fracture with pressure and lode dependence. International Journal of Plasticity 24(6):1071 – 1096

Bao Y, Treitler R (2004) Ductile crack formation on notched Al2024-T351 bars under compression–tension loading. Materials Science and Engineering: A 384(1–2):385–394

Bao Y, Wierzbicki T (2004) On fracture locus in the equivalent strain and stress triaxiality space. International Journal of Mechanical Sciences 46(1):81 – 98

Barsoum I, Faleskog J (2007) Rupture mechanisms in combined tension and shear—Experiments. International Journal of Solids and Structures 44(6):1768 – 1786

Benzerga AA, Surovik D, Keralavarma SM (2012) On the path-dependence of the fracture locus in ductile materials – Analysis. International Journal of Plasticity 37:157 – 170

Bouchard PO, Bourgeon L, Lachapèle H, Maire E, Verdu C, Forestier R, Logé RE (2008) On the influence of particle distribution and reverse loading on damage mechanisms of ductile steels. Materials Science and Engineering: A 496(1–2):223 – 233

Campbell J (2011) The Origin of Griffith Cracks. Metallurgical and Materials Transactions B 42(6):1091–1097

Chen Y, Pedersen KO, Clausen AH, Hopperstad OS (2009) An experimental study on the dynamic fracture of extruded AA6xxx and AA7xxx aluminium alloys. Materials Science and Engineering: A 523(1–2):253 – 262

Christiansen E (2017) Personal communication, Centre for Advanced Structural Analysis (CASA), Norwegian University of Science and Technology (NTNU)

Dæhli LEB, Børvik T, Hopperstad OS (2016) Influence of loading path on ductile fracture of tensile specimens made from aluminium alloys. International Journal of Solids and Structures 88–89:17 – 34

Dowling JM, Martin JW (1976) The influence of MN additions on the deformation behaviour of an Al-Mg-Si alloy. Acta Metallurgica 24(12):1147 – 1153

Drucker DC, Mylonas C, Lianis G (1960) Exhaustion of ductility of E-steel in tension following compressive prestrain. Weld J (Res Suppl) 39:117–120

Enami K (2005) The effects of compressive and tensile prestrain on ductile fracture initiation in steels. Engineering Fracture Mechanics 72(7):1089 – 1105

Faleskog J, Barsoum I (2013) Tension–torsion fracture experiments—Part I: Experiments and a procedure to evaluate the equivalent plastic strain. International Journal of Solids and Structures 50(25–26):4241 – 4257

Gao X, Zhang G, Roe C (2009) A study on the effect of the stress state on ductile fracture. International Journal of Damage Mechanics 19(1):75 – 94

Graham SM, Zhang T, Gao X, Hayden M (2012) Development of a combined tension–torsion experiment for calibration of ductile fracture models under conditions of low triaxiality. International Journal of Mechanical Sciences 54(1):172 – 181

Gruben G, Fagerholt E, Hopperstad OS, Børvik T (2011) Fracture characteristics of a cold-rolled dual-phase steel. European Journal of Mechanics - A/Solids 30(3):204 – 218

Gruben G, Hopperstad OS, Børvik T (2012) Evaluation of uncoupled ductile fracture criteria for the dual-phase steel Docol 600DL. International Journal of Mechanical Sciences 62(1):133 – 146

Hoang NH, Hopperstad OS, Myhr OR, Marioara C, Langseth M (2015) An improved nano-scale material model applied in axial-crushing analyses of square hollow section aluminium profiles. Thin-Walled Structures 92:93 – 103

Khadyko M, Dumoulin S, Børvik T, Hopperstad OS (2014) An experimental–numerical method to determine the work-hardening of anisotropic ductile materials at large strains. International Journal of Mechanical Sciences 88:25–36

Khadyko M, Dumoulin S, Børvik T, Hopperstad OS (2015) Simulation of large-strain behaviour of aluminium alloy under tensile loading using anisotropic plasticity models. Computers & Structures 157:60 – 75

Khadyko M, Marioara CD, Ringdalen IG, Dumoulin S, Hopperstad OS (2016) Deformation and strain localization in polycrystals with plastically heterogeneous grains. International Journal of Plasticity 86:128 – 150

Kristoffersen M, Børvik T, Westermann I, Langseth M, Hopperstad OS (2013) Impact against X65 steel pipes – An experimental investigation. International Journal of Solids and Structures 50(20–21):3430 – 3445

Kristoffersen M, Børvik T, Hopperstad OS (2016) Using unit cell simulations to investigate fracture due to compression–tension loading. Engineering Fracture Mechanics 162:269 – 289

Lloyd DJ (2003) The scaling of the tensile ductile fracture strain with yield strength in Al alloys. Scripta Materialia 48(4):341 – 344

Lohne O, Naess OJ (1979) The Effect of Dispersoids and Grain Size on Mechanical Properties of AlMgSi Alloys. In: Haasen P, Gerold V, Kostorz G (eds) Strength of Metals and Alloys, Pergamon, pp 781 – 788

Ludley JH, Drucker DC (1960) A Reversed Bend Test to Study Ductile to Brittle Transition. The Welding J 39:543s–546s

Maire E, Zhou S, Adrien J, Dimichiel M (2011) Damage quantification in aluminium alloys using in situ tensile tests in X-ray tomography. Engineering Fracture Mechanics 78(15):2679 – 2690

Marcadet SJ, Mohr D (2015) Effect of compression–tension loading reversal on the strain to fracture of dual phase steel sheets. International Journal of Plasticity 72:21 – 43

Morgeneyer TF, Starink MJ, Wang SC, Sinclair I (2008) Quench sensitivity of toughness in an Al alloy: Direct observation and analysis of failure initiation at the precipitate-free zone. Acta Materialia 56(12):2872 – 2884

Papasidero J, Doquet V, Mohr D (2015) Ductile fracture of aluminum 2024-T351 under proportional and non-proportional multi-axial loading: Bao–Wierzbicki results revisited. International Journal of Solids and Structures 69–70:459 – 474

Pedersen KO, Roven HJ, Lademo OG, Hopperstad OS (2008) Strength and ductility of aluminium alloy AA7030. Materials Science and Engineering: A 473(1–2):81 – 89

Pedersen KO, Westermann I, Furu T, Børvik T, Hopperstad OS (2015) Influence of microstructure on work-hardening and ductile fracture of aluminium alloys. Materials & Design 70:31 – 44

Pineau A, Benzerga AA, Pardoen T (2016) Failure of metals I: Brittle and ductile fracture. Acta Materialia 107:424 – 483

Spitzig WA, Richmond O (1984) The effect of pressure on the flow stress of metals. Acta Metallurgica 32(3):457 – 463

Spitzig WA, Sober RJ, Richmond O (1975) Pressure dependence of yielding and associated volume expansion in tempered martensite. Acta Metallurgica 23(7):885 – 893

Thomas N, Basu S, Benzerga AA (2016) On fracture loci of ductile materials under non-proportional loading. International Journal of Mechanical Sciences 117:135 – 151

Toda H, Oogo H, Horikawa K, Uesugi K, Takeuchi A, Suzuki Y, Nakazawa M, Aoki Y, Kobayashi M (2013) The True Origin of Ductile Fracture in Aluminum Alloys. Metallurgical and Materials Transactions A 45(2):765–776

Westermann I, Pedersen KO, Furu T, Børvik T, Hopperstad OS (2014) Effects of particles and solutes on strength, work-hardening and ductile fracture of aluminium alloys. Mechanics of Materials 79:58 – 72

Wilson CD (2002) A critical reexamination of classical metal plasticity. Journal of Applied Mechanics, Transactions ASME 69(1):63–68